

## VARIABILITY OF THE X-RAY P CYGNI LINE PROFILES FROM CIRCINUS X-1 NEAR ZERO PHASE

N. S. SCHULZ<sup>1</sup> AND W. N. BRANDT<sup>2</sup>*Submitted for publication to The Astrophysical Journal*

## ABSTRACT

The luminous X-ray binary Circinus X-1 has been observed twice near zero orbital phase using the High-Energy Transmission Grating Spectrometer (HETGS) onboard *Chandra*. The source was in a high-flux state during a flare for the first observation, and it was in a low-flux state during a dip for the second. Spectra from both flux states show clear P Cygni lines, predominantly from H-like and He-like ion species. These indicate the presence of a high-velocity outflow from the Cir X-1 system which we interpret as an equatorial accretion-disk wind, and from the blueshifted resonance absorption lines we determine outflow velocities of 200–1900 km s<sup>−1</sup> with no clear velocity differences between the two flux states. The line strengths and profiles, however, are strongly variable both between the two observations as well as within the individual observations. We characterize this variability and suggest that it is due to both changes in the amount of absorbing material along the line of sight as well as changes in the ionization level of the wind. We also refine constraints on the accretion-disk wind model using improved plasma diagnostics such as the He-like Mg XI triplet, and we consider the possibility that the X-ray absorption features seen from superluminal jet sources can generally be explained via high-velocity outflows.

*Subject headings:* stars: individual (Cir X-1) — stars: neutron — X-rays: stars — binaries: close — accretion: accretion disks — techniques: spectroscopic

## 1. INTRODUCTION

The discovery of broad P Cygni line profiles from the luminous X-ray binary Circinus X-1 (hereafter Cir X-1), which we reported in Brandt & Schulz (2000; hereafter Paper I), was the first time such lines had been observed clearly in the X-ray spectrum of a cosmic object. The P Cygni lines demonstrated the presence of a high-velocity outflow, in line with other suggestions of outflow in this system (e.g., Johnston, Fender, & Wu 1999). However, the nature of Cir X-1 in general is still poorly understood and, despite advances in recent years, there remains uncertainty about even the most basic properties of this system. Since its discovery (Margon et al. 1971), it has appeared bright and variable in X-rays exhibiting a period of 16.6 days (Kaluzienski et al. 1976), and it has thus been a frequent target of most X-ray observatories. The compact object in the Cir X-1 system is thought to be a neutron star (Tennant, Fabian, & Shafer 1986) that can radiate at super-Eddington luminosities during times of strong mass transfer. Its heavily reddened optical counterpart (e.g., Moneti 1992) shows strong, asymmetric H $\alpha$  emission; this emission is variable and appears to arise from several sites in the system including the accretion disk (e.g., Whelan et al. 1977; Mignani, Caraveo, & Bignami 1997; Johnston et al. 2001). The system shows two arcminute-scale radio jets (Stewart et al. 1993), and an arcsecond-scale asymmetric jet (Fender et al. 1998) suggests the presence of relativistic outflow from the source. Cir X-1 is often included among the “Galactic microquasar” X-ray binaries (Mirabel 2001).

The nature of the companion star is an important issue for the interpretation of the observed X-ray P Cygni lines. Specifically, one must address if the P Cygni lines could be made by absorption of X-rays from the neutron star in a high-velocity wind from the companion; such a scenario is likely for the high-mass X-ray binary Cygnus X-3, which also shows X-ray P Cygni lines (Liedahl et al. 2000) and has a Wolf-Rayet star companion.

ion. The large velocities observed for the X-ray P Cygni lines of Cir X-1 (up to  $\pm 1900$  km s<sup>−1</sup>) would require a high-mass companion, probably of spectral type O.

Several attempts have been made to determine the spectral type of the companion star. While a low-mass companion is favored by most of the recent studies (e.g., Stewart et al. 1991; Glass 1994), the constraints remain weak due largely to the heavy interstellar reddening. Additional evidence for a low-mass companion comes from observations of the correlated X-ray spectral and timing properties, observations of type I X-ray bursts, and theoretical considerations. For example, Shirey, Bradt, & Levine (1999a) and Shirey, Levine, & Bradt (1999b) have demonstrated in extensive studies of *RXTE* data that Cir X-1 exhibits spectral branches in the hardness-intensity diagram that can be identified with the horizontal, normal, and flaring branches of “Z” type low-mass X-ray binaries (LMXBs; e.g., Hasinger & van der Klis 1989; Schulz, Hasinger, & Trümper 1989). Qu, Yu, & Li (2001) have also noted some similarities to the LMXBs GX 5–1 and Cyg X-2. Furthermore, Tauris et al. (1999) considered the (somewhat uncertain) kinematic properties of the Cir X-1 system and argued that the companion is a low-mass ( $\lesssim 2.0 M_{\odot}$ ), unevolved star.

Given that the stellar wind from the likely low-mass companion cannot explain the observed properties of the X-ray P Cygni profiles from Cir X-1, we interpreted these profiles in the context of an equatorial wind driven from the accretion disk by a combination of Compton heating and radiation pressure (see Paper I). The fact that Cir X-1 can radiate with high luminosity relative to its Eddington luminosity ( $L/L_{\text{Edd}}$ ) makes it a natural system in which to expect observable outflows, because of the larger amount of photon pressure available per unit gravitational mass. Accretion-disk winds in X-ray binaries have been discussed both theoretically and observationally (e.g., Begelman, McKee, & Shields 1983; Raymond 1993; Chiang 2001;

<sup>1</sup>Center for Space Research, Massachusetts Institute of Technology, Cambridge, MA 02139.<sup>2</sup>Department of Astronomy & Astrophysics, 525 Davey Laboratory, The Pennsylvania State University, University Park, PA, 16802.

Proga & Kallman 2001), and the P Cygni lines seen from Cir X-1 match the lines predicted by Raymond (1993) reasonably well. We also note that Iaria et al. (2001a, 2001b) have recently found evidence for a large column density of ionized gas along the line of sight based on observations of ionized iron K edges; the same gas might well produce both the X-ray P Cygni lines and the ionized iron K edges.

P Cygni lines are a common property of the ultraviolet spectra of cataclysmic variables (CVs) possessing an accretion disk. In these systems, the line profiles are associated with high-velocity polar outflows (e.g., Córdova & Howarth 1987), in contrast to the equatorial geometry proposed for the accretion-disk wind in Cir X-1. The proposed equatorial geometry was motivated by evidence that the Cir X-1 system is viewed in a relatively edge-on manner. Although eclipses are not observed, the spectral variability caused by the observed X-ray absorption is best explained by a model with a relatively edge-on accretion disk (Brandt et al. 1996; Shirey et al. 1999b). In this model, X-rays created near the neutron star reach the observer via two light paths: (1) a direct, but often absorbed, light path that can intersect the outer bulge of the accretion disk, and (2) an indirect, electron-scattered light path that avoids the absorption associated with the direct light path. This model can naturally explain the large observed changes in the column density of the absorbing gas without corresponding changes in its apparent covering fraction (see Brandt et al. 1996 for details). We note that radio imaging of SS433, which shares several similarities with Cir X-1, provides strong evidence for an equatorial wind-like outflow from this system (Blundell et al. 2001).

In this second paper, we present results from a variability study of the X-ray P Cygni lines from Cir X-1. As in Paper I the observations were performed with the High-Energy Transmission Grating Spectrometer (HETGS) onboard *Chandra* at “zero phase.” Zero phase in Cir X-1 is thought to be associated with the periastron passage of the neutron star, and near this phase Cir X-1 is highly variable in X-ray intensity. We present analyses of two observations, which include a re-assessment of the data presented in Paper I representing a high-flux state of Cir X-1 and a second observation during which Cir X-1 was in a low-flux state with strong variability. In Schulz & Brandt (2001; hereafter SB2001) we already presented a broad-band continuum fit to some of the data as well as showed temporal changes of the Si XIV line. The analysis here focuses on a comparison of the bright lines in the two zero-phase flux states and their variability with intensity and time.

Throughout this paper, we adopt a distance to Cir X-1 of 6 kpc (Stewart et al. 1993; Case & Bhattacharya 1998) and an interstellar column density of  $2 \times 10^{22} \text{ cm}^{-2}$  (e.g., Predehl & Schmitt 1995).

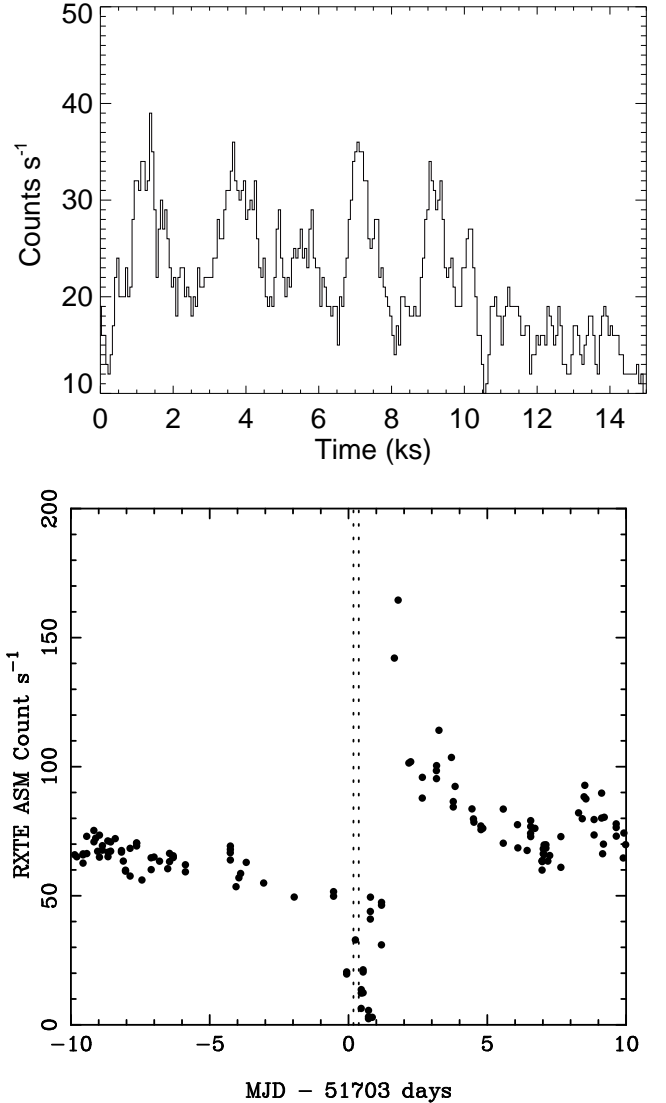


FIG. 1.— The top panel shows the 1st order light curve of observation II in 60 s bins. The bottom panel shows the RXTE ASM light curve including 10 days before and after observation II was performed with *Chandra* (the *Chandra* observation window is marked by dotted lines). A similar plot for observation I can be found in Paper I.

## 2. CHANDRA OBSERVATIONS

Cir X-1 was observed with the *Chandra* HETGS (C.R. Canizares et al., in preparation) on 2000 February 29 (starting at 22:09:50 UT) for 30 ks (observation I) and on 2000 June 8 (starting at 04:13:01 UT) for another 15 ks (observation II).<sup>3</sup> Both observations were performed near zero phase of the binary orbit. They were not precisely at the same phase; observation I started at phase 0.9917, and observation II started at phase 0.9923 (adopting the ephemeris of Glass 1994). In Paper I we showed that observation I occurred during the onset of a luminous flare. Figure 1 puts observation II similarly into perspective with the long-term RXTE ASM light curve. Here it appears that we observed the source during a prominent intensity dip. Observation I is also different from observation II because it suffered from a misalignment of the applied subarray during the observation which led to the loss of half of the data. Otherwise observation II was performed with a similar instrumental setup; the zeroth order was blocked from being telemetered, and the same subarray with CCDs S0 and S5 inactive was

<sup>3</sup>For details on *Chandra* and the HETGS see the *Chandra* Proposers’ Observatory Guide at <http://asc.harvard.edu/udocs/docs/>.

applied leading to a frame time of 1.7 s.

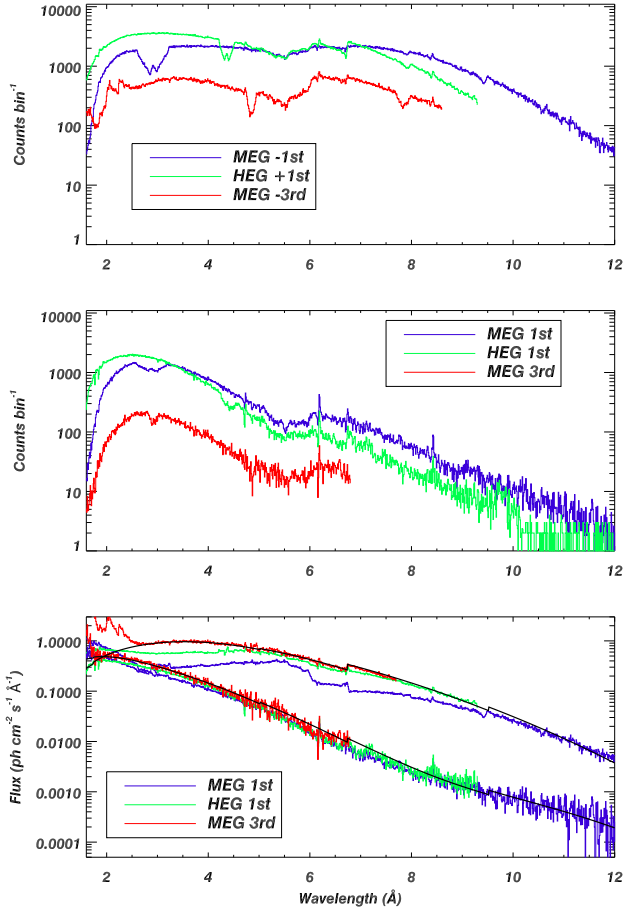


FIG. 2.— The raw-count spectra of observation II (top) and observation I (middle) plotted on the same scale. The MEG 1st order spectra are blue, the HEG 1st order spectra are green, and the MEG 3rd order spectra are red. The bottom panel shows these corrected for exposure. The brighter set corresponds to observation I, and the fainter set corresponds to observation II.

### 2.1. Raw-count spectra

Observation I was the basis for the discovery of the P Cygni profiles, and most of its basic properties were described in Paper I. We reprocessed these data using several improved calibration data products. The first one concerns a small correction to the wavelength scale, which arose from a re-assessment of the detector pixel size and which led to a scale factor of 500 ppm in the wavelength scale. This leads to a maximal difference of 0.0075 Å at 15 Å compared to the previous definition. For shorter wavelengths this change is of the order of the previous accuracy of the wavelength determination. A second change came from the application of the CCD quantum efficiency, which has now been provided with a finer energy grid. The benefits here are that instrumental edges, for our interest especially the CCD Si-edge, have been accounted for more accurately and are less likely to produce spectral artifacts. A third improvement came from correction of a slight mismatch of the energy grids in the ancillary data files and the grating response. All data were processed the same way with the exception that in observation II we additionally added positive and negative orders together. In this respect we re-gained essentially the same exposure as in observation I. The raw-count spectra in Figure 2 (top) indicate a very high number of counts during observation I. The MEG 1st order spectra have  $1.4 \times 10^6$  events, the HEG 1st order spectra have  $1.5 \times 10^6$  events, and the MEG 3rd

order spectra have  $3.9 \times 10^5$  events.

In observation II (middle) the MEG 1st order spectra have  $3.3 \times 10^5$  events, the HEG 1st order spectra have  $2.1 \times 10^5$  events, and the MEG 3rd order spectra have  $4.0 \times 10^4$  events. The difference in intensity is well illustrated by the raw-count spectra shown in Figure 2. Throughout most of the spectral bandpass, the number of counts in observation II is significantly lower in each bin compared to observation I. This had the favorable effects that we did not suffer from any frame dropouts during data transmission and were much less affected by pile-up. The number of counts per bin in observation II drops below  $\approx 1$  above 12 Å, which basically reflects the noise level. In Figure 2 we therefore terminate the spectra at 12 Å for better visibility of the details at shorter wavelengths, although the MEG spectrum in observation I continues up to 15.5 Å (see Paper I).

### 2.2. Pile-up issues

The amount of pile-up in the spectra makes detailed modeling of the X-ray continuum difficult. Pile-up affects the MEG and HEG spectra over a considerable bandpass where the number of incident counts per frame in a given pixel is very high. In order to get a lower limit of the number of detected counts per frame and pixel a rough estimate of its dependence on wavelength, one can divide the count spectra in Figure 2 by the number of CCD frames obtained during the observation period and the number of pixels included in each bin. Values significantly above 0.01 indicate that the spectra are likely affected by pile-up. In general to obtain more precise information there is no straightforward procedure, but there are several other leads that allow one to identify pile-up affected regions in the spectra. High photon densities are only reached in the 1st orders where the effective area of the instrument is highest. In the MEG 1st order spectrum this happens below  $\sim 11$  Å, while in the HEG 1st order spectrum it happens below  $\sim 8$  Å. All higher orders are not affected by pile-up. However, they still suffer from contamination of piled-up photons from the 1st orders. Pile-up in the 1st orders creates a depletion of photons at a specific wavelength. Since it is a CCD effect, multiple photon coincidences appear in higher CCD channels since they are recorded as an event that has the sum of the incident energies. In the HETGS these channels also coincide with the locations of the higher order grating spectra. In this respect three first-order photons, for example, appear as one photon in 3rd order at 1/3 of the original wavelength. This means that the MEG 3rd order below  $\sim 2$  Å is contaminated by pile-up from the MEG 1st order. Since no viable model yet exists to correct for this effect, we will avoid all areas in the spectra that suffer substantially from pile-up. In the MEG 1st order the range below 2 Å is also affected by some contamination from zero-order scattering and is excluded as well. For observation I, for example, this leaves the following wavelength bands for spectral modeling: 2.4–8.5 Å in the MEG 3rd order, 8.2–10.1 Å in the HEG 1st order, and above 11 Å in the MEG 1st order. The wavelength range below 2 Å in the HEG 1st order is mildly affected by pile-up, and here we have to add corrections (see §3.5). The available energy bands are thus 0.8–5.2 keV and 6.2–8 keV. Observation II shows considerably lower count rates, and its spectra are much less affected by pile-up and zero-order scattering; here we can use almost the entire 1.0–8.0 keV energy band.

Figure 2 (bottom) shows the exposure-corrected spectra for observations I and II. The top set of spectra with the higher

fluxes are from observation I, and the bottom set are from observation II. The spectra are integrated over the entire exposures. Without pile-up the blue, green and red spectra of both sets should overlap. This qualitatively gives an impression of the degree of pile-up, which is indicated by how much the blue and green spectra deviate from the red spectra.

For the analysis of the lines we mostly rely on the HEG 1st order spectra for statistical reasons. This requires some corrections in areas where pile-up appears strong, which is between 2 and 7 Å. From the difference of the exposure-corrected spectra and the pile-up free 3rd order spectra we can determine an energy dependent flux correction factor, which we later use to correct the equivalent widths of the lines. The model of the HEG 1st order spectrum of observation II in Figure 3 has these factors applied, and the figure shows that we get good agreement. The additional systematic uncertainty in the determination of equivalent widths can be up to 20% is the worst case.

### 2.3. Determining fluxes and luminosities

In general we follow the procedure to determine the luminosity outlined in SB2001 and choose our model spectrum from previous fits to ASCA data (Brandt et al. 1996); the model consisted of two blackbody components with both intrinsic partial-covering absorption and interstellar absorption of  $2.0 \times 10^{22} \text{ cm}^{-2}$  using cross-sections from Morrison & McCammon (1983). The two observations can be compared to the low-count-rate state (observation II) and high-count-rate state (observation I) in Brandt et al. (1996). We emphasize, however, that the current HETGS spectra do not qualify for a detailed physical discussion of the continuum, and we use the fits mainly as a parameterization of the continuum emission in order to perform the line analysis. We also draw some basic information from the change of the fits from observation I to observation II.

For observation I we find a soft blackbody temperature of  $kT = 0.66 \pm 0.17 \text{ keV}$  [partial covering  $N_{\text{H}} = (8.2 \pm 0.4) \times 10^{23} \text{ cm}^{-2}$ ] and a hard blackbody temperature of  $kT = 1.22 \pm 0.28 \text{ keV}$  [partial covering  $N_{\text{H}} = (2.3 \pm 0.2) \times 10^{22} \text{ cm}^{-2}$ ]; the partial covering fraction was 45%. We find a total absorbed X-ray flux of  $2.0 \times 10^{-8} \text{ erg cm}^{-2} \text{ s}^{-1}$  with the soft component contributing 61% between 2–8 keV. This corresponds to a luminosity of  $1.8 \times 10^{38} \text{ erg s}^{-1}$ . During observation II we could fix the the partial covering columns to the values found in observation I; we find a covering fraction of 89%. The temperature for the soft blackbody component was  $kT = 0.16 \pm 0.09 \text{ keV}$ , and for the hard blackbody component it was  $kT = 1.55 \pm 0.21 \text{ keV}$ . The total absorbed X-ray flux dropped to  $4.8 \times 10^{-9} \text{ erg cm}^{-2} \text{ s}^{-1}$  with a contribution of the soft component of < 1%. The corresponding luminosity is  $2.8 \times 10^{37} \text{ erg s}^{-1}$ . We emphasize again that the model parameters we have empirically derived to parameterize the continuum are not optimal for comparison with previous results (Brandt et al. 1996; Shirey et al. 1999). A full pile-up model will be required for detailed HETGS continuum fitting, and even then the limited high-energy sensitivity will remain an obstacle. As we discuss in §3.5, the correction for absorption during observation II is generally uncertain, and hence the true luminosity of Cir X-1 is difficult to constrain during this observation. It is plausible that the true luminosity during observation II is comparable to that during observation I. Such behavior would be consistent with that observed by ASCA (Brandt et al. 1996) and RXTE (Shirey et al. 1999b) during dips. Evidence for heavy and complex absorption in the *Chandra* data is found in

the depths of the neutral Fe K (see §3.5) and maybe the Si K edges. Both observations show a neutral Si K edge with a depth of  $\tau = 0.15$ . The large depth of this edge required us to add an additional edge to our fits. However, although current uncertainties in the improved instrument efficiencies cannot account for such a large effect, it was also observed recently in HETGS spectra of other bright sources (Miller et al. 2002).

## 3. P CYGNI LINE ANALYSIS

### 3.1. Basic line measurements

For the line analysis we binned all spectra into 0.005 Å bins (which oversamples the HEG resolution by a factor of two). All the analysis in this section has been performed on the raw data. The spectra are integrated over the entire exposure. We use lines detected in the HEG 1st and MEG 3rd orders, except in observation I where we use the MEG 1st order above 10 Å. We detect a number of resonance line features in both observations, of which the brightest clearly show P Cygni profiles (Paper I). Figure 3 shows the spectrum of observation II from 1.7–9 Å with all identified features marked. Table 1 includes all line features detected with a signal-to-noise ratio larger than three for both observations. Most of the lines are from H-like and He-like species, although we do detect some Li-like and B-like species from elements with high atomic numbers. For some of the lines the P Cygni shape is less pronounced, and we find them either mostly in emission or absorption (see below). Notable in observation II is the detection of the forbidden line of He-like Mg XI, which cannot appear as a P Cygni line since it is not a dipole transition.

Table 1 lists each ion in column 1, the transition name in column 2 (“H-like” denotes ions with only one electron left, “He-like” with two, and so on), and the predicted wavelength from the SPEX (Mewe 1994) line list in column 3. In column 4 we list the measured wavelength, which represents the intersection between the emission and the absorption with the continuum. The intersection with the continuum is generally a good estimate of the rest-wavelength position. This is underlined by the fact that on average the profiles appear symmetric. In order to quantify the properties of the P Cygni lines, we normalized each profile by dividing the data by the underlying local continuum (where we simply applied a polynomial fit) and then fitted the absorption and emission components with Gaussians. Within the statistical uncertainties, simple Gaussian functions proved to be sufficient for the fits. The velocities listed in column 5 represent the difference between the measured wavelength and the peak position of the Gaussian fitting the absorption part of the line (note, of course, that the maximum velocity to which absorption is observed is higher than this); lines without clear P Cygni shapes do not have velocity values listed. Most emission peaks appear slightly above the expected wavelength in column 3; in a few cases they match well, and here we have probably slightly underestimated the velocity. We find velocities of 200–1900 km s<sup>-1</sup>.

We determined the equivalent widths of the lines from the fits. They are listed in column 6 of Table 1. The values are measured from HEG 1st order data unless noted otherwise. The equivalent width of a P Cygni line,  $W_{\text{pc}}$ , is defined as the sum of the equivalent widths of the emission and the absorption (taking both to be positive quantities). For the analysis below we also list the contribution of absorption as a fraction of  $W_{\text{pc}}$  ( $f_a$  in column 7 of Table 1). The Fe-line area below 2 Å is treated separately below.

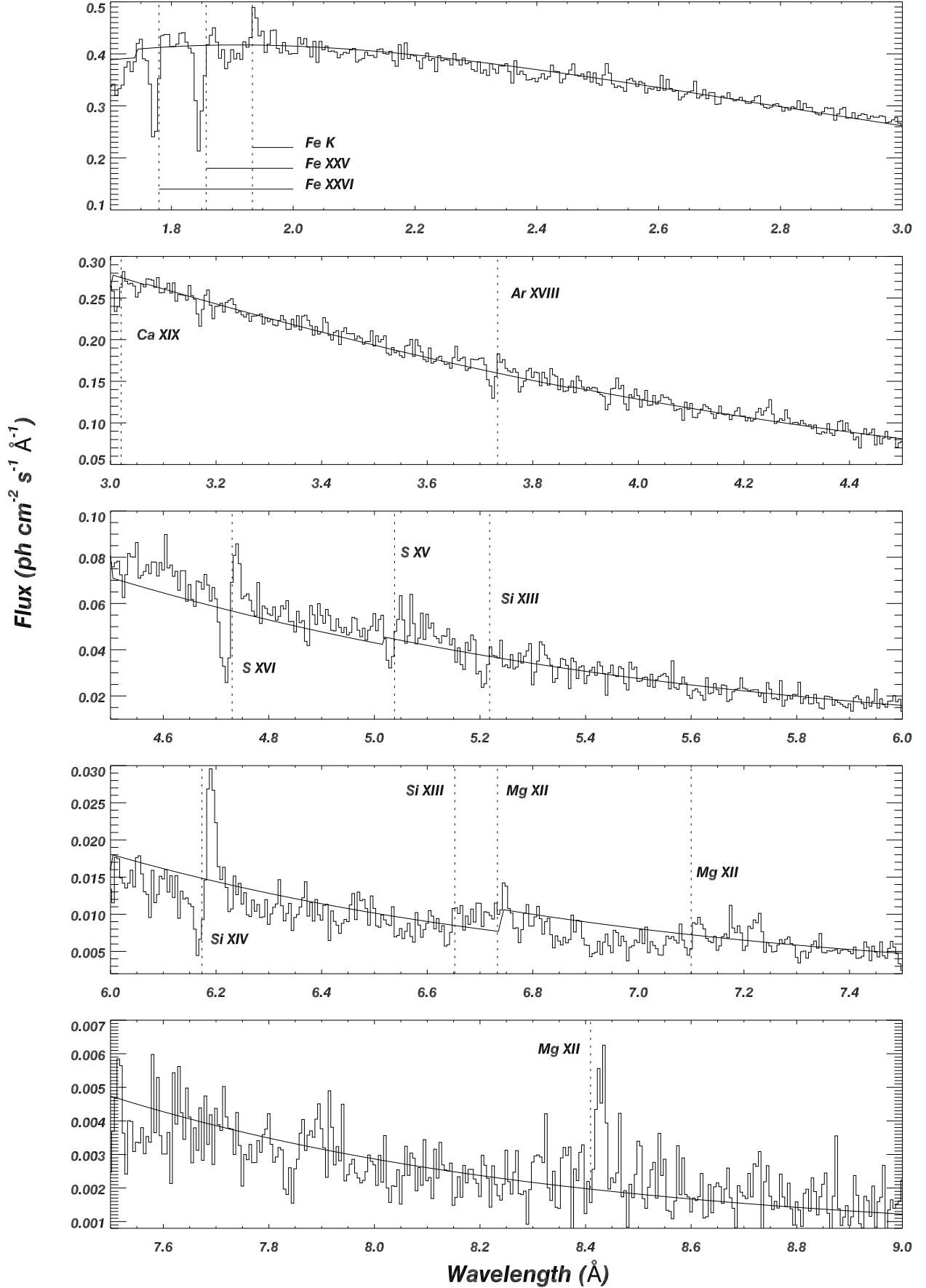


FIG. 3.— The co-added HEG 1st order spectrum from observation II up to 9 Å with all identified spectral features marked. The two-blackbody model described in §2.3 is also plotted, after we applied an empirical correction for pile-up (see §2.2).

TABLE 1  
LINE IDENTIFICATIONS AND PROPERTIES

Ion (1)	Transition <sup>a</sup> (2)	Predicted $\lambda$ (Å) (3)	Measured $\lambda$ (Å) (4)	$v$ (km s <sup>-1</sup> ) (5)	$W_{pc}$ (mÅ) (6)	$f_a$ (7)	$N_{abs}$ ( $\times 10^{16}$ cm <sup>-2</sup> ) (8)	$F_{el}$ ( $\times 10^{-4}$ ph cm <sup>-2</sup> s <sup>-1</sup> ) (9)
Observation I								
Fe XXVI	H-like (Ly $\alpha$ )	1.78	1.7792 $\pm$ 0.0013	1010 $\pm$ 340	3.93 $\pm$ 0.23	0.25	8.57	15.53 $\pm$ 1.25
Fe XXV	He-like	1.85	1.8543 $\pm$ 0.0014	1940 $\pm$ 320	6.27 $\pm$ 0.31	0.48	12.60	21.54 $\pm$ 1.75
Ar XVIII	H-like (Ly $\alpha$ )	3.73	3.7291 $\pm$ 0.0021	320 $\pm$ 160	3.26 $\pm$ 0.25	0.46	3.96	11.64 $\pm$ 1.42
S XV	He-like	4.31	4.3526 $\pm$ 0.0024	1860 $\pm$ 140	13.53 $\pm$ 0.37 <sup>b</sup>	...	...	...
S XVI	H-like (Ly $\alpha$ )	4.73	4.7252 $\pm$ 0.0026	820 $\pm$ 130	4.51 $\pm$ 0.34	0.44	3.36	16.84 $\pm$ 2.00
Si XIV	H-like (Ly $\delta$ )	4.85	4.8571 $\pm$ 0.0026	60 $\pm$ 120	1.70 $\pm$ 0.22	...	...	8.11 $\pm$ 1.28
Si XIV	H-like (Ly $\gamma$ )	4.95	4.9467 $\pm$ 0.0027	240 $\pm$ 120	1.40 $\pm$ 0.21	...	...	6.02 $\pm$ 1.23
S XV	He-like (r)	5.04	5.0333 $\pm$ 0.0027	300 $\pm$ 120	2.81 $\pm$ 0.24	0.64	1.41	6.52 $\pm$ 1.37
Si XIV	H-like (Ly $\beta$ )	5.22	5.2080 $\pm$ 0.0028	340 $\pm$ 110	2.21 $\pm$ 0.26	0.68	5.25	4.10 $\pm$ 1.32
Si XIV	H-like (Ly $\alpha$ )	6.18	6.1816 $\pm$ 0.0032	480 $\pm$ 180	12.03 $\pm$ 0.84 <sup>c</sup>	0.42	3.59	15.64 $\pm$ 0.95
Mg XII	H-like (Ly $\gamma$ )	6.74	6.7338 $\pm$ 0.0035	760 $\pm$ 90	3.49 $\pm$ 0.30 <sup>c</sup>	0.46	13.77	9.94 $\pm$ 0.67
Mg XII	H-like (Ly $\beta$ )	7.10	7.0902 $\pm$ 0.0038	...	1.12 $\pm$ 0.44	...	...	5.48 $\pm$ 0.58
Fe XXIV	Li-like	7.36	7.3613 $\pm$ 0.0037	...	1.04 $\pm$ 0.41	...	...	4.81 $\pm$ 0.57
Ni XXIV	B-like	7.55	7.5623 $\pm$ 0.0038	...	1.05 $\pm$ 0.41	...	...	4.30 $\pm$ 0.55
Mg XII	H-like (Ly $\alpha$ )	8.42	8.4080 $\pm$ 0.0043	710 $\pm$ 70	9.78 $\pm$ 0.75	0.49	1.83	4.80 $\pm$ 0.62
Mg XI	He-like (i)	9.23	9.2139 $\pm$ 0.0047	460 $\pm$ 70	7.01 $\pm$ 1.36	0.46	...	1.71 $\pm$ 0.53
Ne X	H-like (Ly $\delta$ )	9.48	9.4891 $\pm$ 0.0048	220 $\pm$ 60	7.02 $\pm$ 1.24	0.43	27.12	1.85 $\pm$ 0.49
Fe XXIV	Li-like	10.63	10.6341 $\pm$ 0.0098	1130 $\pm$ 170	6.77 $\pm$ 1.01 <sup>d</sup>	0.49	0.85	1.45 $\pm$ 0.45
Ne X	H-like (Ly $\alpha$ )	12.13	12.1082 $\pm$ 0.0102	740 $\pm$ 70	11.23 $\pm$ 1.25 <sup>d</sup>	0.44	0.91	2.52 $\pm$ 0.48
Observation II								
Fe XXVI	H-like (Ly $\alpha$ )	1.78	1.7796 $\pm$ 0.0013	1010 $\pm$ 340	6.39 $\pm$ 0.25	0.85	36.23	3.35 $\pm$ 1.15
Fe XXV	He-like	1.85	1.8570 $\pm$ 0.0014	1940 $\pm$ 320	6.89 $\pm$ 0.29	0.76	21.88	5.73 $\pm$ 1.76
Ca XIX	He-like (r)	3.04	3.0201 $\pm$ 0.0018	890 $\pm$ 200	3.13 $\pm$ 0.30	0.72	6.61	2.22 $\pm$ 0.66
Ar XVIII	H-like (Ly $\alpha$ )	3.73	3.7333 $\pm$ 0.0021	640 $\pm$ 160	5.56 $\pm$ 0.42	0.59	6.40	3.40 $\pm$ 0.54
S XVI	H-like (Ly $\alpha$ )	4.73	4.7304 $\pm$ 0.0026	760 $\pm$ 130	25.07 $\pm$ 1.13	0.58	17.65	6.15 $\pm$ 0.57
S XV	He-like (r)	5.04	5.0381 $\pm$ 0.0027	600 $\pm$ 120	7.42 $\pm$ 1.33	0.47	2.02	1.41 $\pm$ 0.41
Si XIV	H-like (Ly $\beta$ )	5.22	5.2182 $\pm$ 0.0028	800 $\pm$ 110	10.63 $\pm$ 1.22	0.91	26.04	0.37 $\pm$ 0.38
Si XIV	H-like (Ly $\alpha$ )	6.18	6.1783 $\pm$ 0.0032	440 $\pm$ 100	49.63 $\pm$ 1.77	0.36	12.71	3.14 $\pm$ 0.15
Si XIII	He-like (r)	6.65	6.6522 $\pm$ 0.0035	630 $\pm$ 90	14.79 $\pm$ 2.09	0.64	3.19	0.41 $\pm$ 0.14
Mg XII	H-like (Ly $\gamma$ )	6.74	6.7330 $\pm$ 0.0035	...	8.27 $\pm$ 1.49	...	...	0.48 $\pm$ 0.10
Mg XII	H-like (Ly $\beta$ )	7.10	7.1000 $\pm$ 0.0037	200 $\pm$ 80	16.04 $\pm$ 3.09	0.44	20.02	0.40 $\pm$ 0.12
Mg XII	H-like (Ly $\alpha$ )	8.42	8.4094 $\pm$ 0.0043	710 $\pm$ 70	35.59 $\pm$ 4.87	0.32	4.36	0.40 $\pm$ 0.09
Mg XI	He-like (r)	9.17	9.1700 $\pm$ 0.0047	...	12.03 $\pm$ 4.50	...	...	0.15 $\pm$ 0.06
Mg XI	He-like (i)	9.23	9.2319 $\pm$ 0.0047	...	14.29 $\pm$ 4.35	...	...	0.21 $\pm$ 0.08
Mg XI	He-like (f)	9.31	9.3088 $\pm$ 0.0048	...	14.79 $\pm$ 5.99	...	...	0.23 $\pm$ 0.08
Ne X	H-like (Ly $\delta$ )	9.48	9.4861 $\pm$ 0.0048	...	17.29 $\pm$ 4.76	...	...	0.14 $\pm$ 0.06

<sup>a</sup>From Mewe (1994).

<sup>b</sup>Affected by a chip gap, and results are unreliable.

<sup>c</sup>Added from MEG 3rd order.

<sup>d</sup>Added from MEG 1st order.

### 3.2. High-flux versus low-flux states

In this section we analyze the variations of the P Cygni lines between observation I and observation II. The measured wavelengths (as well as the ones for the peak and valley positions) of the same transitions in both observations agree to within the stated uncertainties. The most dramatic change is observed in the equivalent widths of the lines. In Figure 4 we compare the P Cygni profiles for the lines with the highest equivalent widths in both observations, which are the Lyman  $\alpha$  lines of S XVI (left), Si XIV (middle), and Mg XII (right). Pile-up effects for S XVI and Si XIV cannot account for the strong variability of the lines. The equivalent widths in observation I are generally lower than in observation II throughout the whole bandpass. The equivalent widths of the three Lyman  $\alpha$  lines in Figure 4 differ by a factor of  $\approx 4$ , whereas the other lines typically differ by a factor of  $\approx 2$ .

### 3.3. Emission lines

The fluxes of the emission lines are shown in column 9 of Table 1. The lines in observation I appear bright with fluxes from  $1.5 \times 10^{-4}$  ph cm $^{-2}$  s $^{-1}$  at 10.63 Å to  $2.2 \times 10^{-3}$  ph cm $^{-2}$  s $^{-1}$  at 1.85 Å. The general trend of declining line flux with increasing wavelength is largely due to absorption by the interstellar column density. The brightest lines appear to be the Lyman  $\alpha$  lines of Fe XXVI, S XVI, and Si XIV, as well as He-like Fe XXV. In observation II the lines' fluxes dropped significantly to a range from  $1.5 \times 10^{-5}$  ph cm $^{-2}$  s $^{-1}$  to  $6.2 \times 10^{-4}$  ph cm $^{-2}$  s $^{-1}$ . There is a trend for the largest decline in line flux to happen toward longer wavelengths; above 6.5 Å the decline is  $\approx 12$ –20 while below 5 Å the decline is  $\approx 3$ –5.

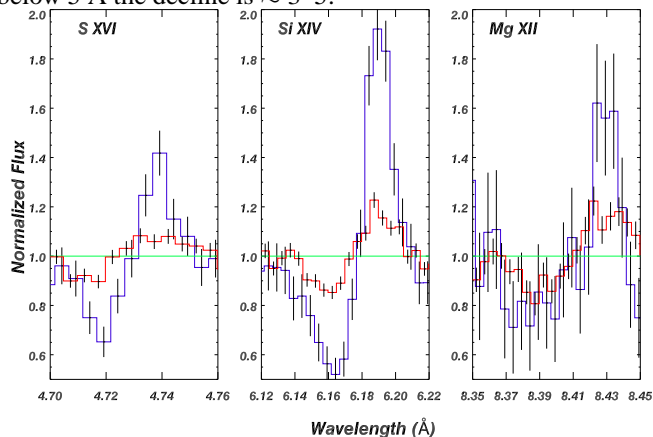


FIG. 4.— Relative P Cygni line strengths of the Lyman  $\alpha$  transitions in S XVI, Si XIV, and Mg XII for observation I (red) and observation II (blue).

Of particular interest is the He-like Mg XI triplet, because it is the only one we can clearly resolve and appears free of contaminating features; for comparison, the Si XIII triplet is confused with the Mg XII Lyman  $\gamma$  line as well as the Si K edge. He-like triplets are sensitive to temperature and density and thus can be used as plasma diagnostics; we use the calculations by Porquet & Dubau (2000). Calculation of the  $G = (i+f)/r$  ratio ( $i$  is the flux of the intercombination line,  $f$  the flux of the forbidden line, and  $r$  the flux of the recombination line) and  $R = i/f$  ratio allows estimation of the temperature and density, respectively (Gabriel & Jordan 1969). Our best constraints come from observation II since during this observation we detect all the lines in the triplet as shown in Figure 5. We compute a  $G$  ratio of  $2.9 \pm 1.0$  and an  $R$  ratio of  $1.1 \pm 0.34$ , implying a temperature

of  $(3.8 \pm 1.1) \times 10^6$  K and a density of  $(1.9 \pm 0.9) \times 10^{13}$  cm $^{-3}$ . A  $G$  ratio of  $\approx 3$  indicates a photoionized plasma dominated by recombination (Bautista & Kallman 2000) and justifies the use of the Porquet & Dubau (2000) calculations, which are specifically designed for a recombining plasma. During observation I we only detect the intercombination line at 9.23 Å and use the  $1\sigma$  uncertainty in the continuum as an upper limit for the detection of the forbidden and resonance lines. We estimate an  $R$  ratio of  $> 0.5$ , implying a density of  $< 4 \times 10^{13}$  cm $^{-3}$ . The  $G$  ratio is not well constrained during observation I.

Figure 5 shows that the Mg XI triplet probably does not suffer from blending, which would mainly stem from possible lower-shell absorption events. These are unlikely given the high ionization states observed. Fe L emission lines are unlikely to appear as blends, because Kallman et al. (1996) predicted that recombination emission is dominated by K-shell ions and not L-shell ions. We cannot exclude the possibility that resonance scattering affects the line ratios; this would tend to increase the flux of the resonance line and thus lower the  $G$  ratio. The consequence would be that the temperature is higher or, in the extreme case, that the Porquet & Dubau (2000) calculations are not applicable because the plasma is not predominately recombining. However, the resonance line does not appear very strong in the spectrum, and a correction of  $G$  due to resonance scattering seems unlikely to be highly significant.

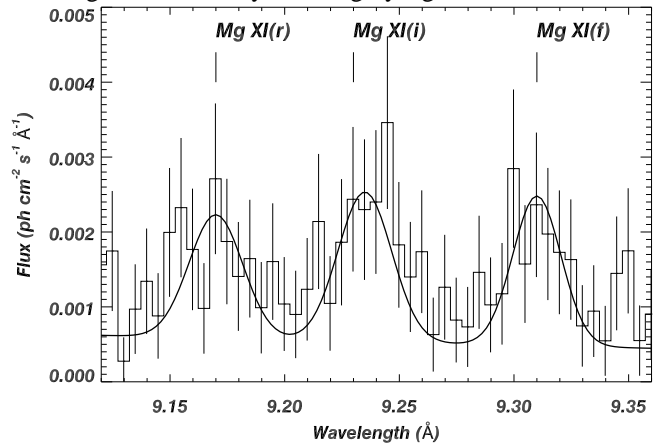


FIG. 5.— The He-like Mg XI triplet in observation II with resonance (r), intercombination (i), and forbidden (f) lines.

### 3.4. Absorption column densities

The measurements of the absorption-line equivalent widths allow estimation of the ionic column densities in the absorbing medium. For an absorption line on the linear part of the curve of growth, the relation between equivalent width and column density is

$$\frac{W_\lambda}{\lambda} = \frac{\pi e^2}{m_e c^2} N_j \lambda f_{ij} = 8.85 \times 10^{-13} N_j \lambda f_{ij} \quad (1)$$

where  $N_j$  is the column density of ion species  $j$ ,  $f_{ij}$  is the oscillator strength of the transition, and  $W_\lambda$  is the equivalent width of the absorption line (e.g., Spitzer 1978; see also Lee et al. 2001). In Table 1 we list the column density,  $N_{\text{abs}}$ , for each ion species derived using this formula.

Several effects may lead to systematic underestimates of column densities when the formula above is used. Given the observed P Cygni profiles, for example, it is likely that line emission fills in some of the absorption; it is difficult to correct for

the resulting column-density underestimates precisely. Furthermore, line saturation can also lead to an underestimate of the column density. The observed lines could be saturated even though they do not appear “black” because of multiple light paths to the observer (e.g., the electron scattering of some X-rays around the absorbing material; see §1). The observed lines might also have unresolved substructure composed of narrower, saturated lines. In fact, since we observe lines from high-order transitions in the Lyman series, the Lyman  $\alpha$  lines are probably saturated; the oscillator strengths decrease by a factor of  $\approx 30$  from the 1s-2p (Lyman  $\alpha$ ) to the 1s-4p (Lyman  $\delta$ ) transitions. We therefore see the column densities in Table 1 more as lower limits, and we note that the column densities derived from the high-order Lyman transitions probably have the least systematic error. For the determination of column densities we thus rely only on the highest-order Lyman transition detected.

In order to estimate equivalent hydrogen column densities, we must correct for the ionization fraction of a given ion. From the analysis of the Mg XI triplet, it is likely that we observe a photoionized plasma. In the following we use the calculations by Kallman & Bautista (2001) for such a plasma which provide a representative ionization structure. For a temperature of  $3.8 \times 10^6$  K (see §3.3), we find an ionization parameter of  $\xi = L/nR^2 \approx 20,000$  erg cm s $^{-1}$ , which is consistent with the fact that we observe mostly H-like ions. We find a similar value of  $\xi$  when we compare our abundance ratios [AR= $N_{\text{abs}}(\text{H-like})/N_{\text{abs}}(\text{He-like})$ ] with their calculations. Table 2 shows the ionization fractions for Mg, Si, S, and Fe and the derived equivalent hydrogen column densities as determined from the observed abundance ratios; the column densities are given for both a solar-abundance distribution from Morrison & McCammon (1983) and an interstellar-abundance distribution from Wilms, Allen, & McCray (2000).

The equivalent hydrogen column densities in Table 2 appear to increase significantly between observation I and observation II. However, as discussed in §3.3, we only have limited constraints on the ionization structure of the gas during observation I because we do not detect all the lines in the Mg XI triplet. We cannot rule out, for example, a reduction in the ionization fraction during observation II that explains all the observed changes. Some of the derived column densities should be taken with caution. It is unusual, for example, that we observe a strong Mg XII 1s-3p transition, whereas the 1s-2p transition is missing. In fact if we discard the result for this line, the derived column density using Mg would be similar to those computed using the other elements.

TABLE 2  
IONIZATION FRACTIONS AND EQUIVALENT HYDROGEN  
COLUMN DENSITIES

Ion	AR <sup>a</sup>	$f_{\text{ion}}^{\text{b}}$	$N_{\text{H}}^{\text{c}}$ ( $10^{22}$ cm $^{-2}$ )			$N_{\text{H}}^{\text{c}}$ ( $10^{22}$ cm $^{-2}$ )
				Observation I	Observation II	
Fe XXVI	0.68	0.327	1.5 (1.9)	1.7	0.491	4.6 (5.6)
Fe XXV	...	0.514	...	...	0.277	...
S XVI	2.4	0.480	0.7 (1.1)	8.7	0.290	6.4 (9.9)
S XV	...	0.199	...	...	0.032	...
Si XIV	5.1 <sup>d</sup>	0.310	0.7 (1.4)	8.2	0.244	7.9 (15.8)
Si XIII	...	0.035	...	...	0.019	...
Mg XII	14.5 <sup>d</sup>	0.237	3.0 (4.7)	22.4 <sup>d</sup>	0.162	7.2 (11.5)
Mg XI	...	0.016	...	...	0.007	...

<sup>a</sup> $N_{\text{abs}}(\text{H-like})/N_{\text{abs}}(\text{He-like})$

<sup>b</sup>Ionization fractions from Kallman & Bautista (2001).

<sup>c</sup>Equivalent hydrogen column density for a solar-abundance distribution (Morrison & McCammon 1983) and an interstellar-abundance distribution (Wilms, Allen, & McCray 2000; in parentheses).

<sup>d</sup>Estimated lower limits.

### 3.5. The Fe K line region

The Fe K line region is especially interesting for spectroscopy because Fe has quite high fluorescent yields (Auger destruction is not as dominant as in lower  $Z$  elements) as well as ions that can survive at high ionization parameters. Figure 6 (top) shows the Fe K region from 1.7–2.0 Å as observed with the HEG during observation I. The model (red curve) includes the continuum level as fitted over the entire available bandpass (see §2.3). In addition we applied an empirical correction to account for pile-up (see §2.2) which we computed by matching featureless continuum stretches in the 1.97–3.00 Å range. Below 1.97 Å additional Gaussians were fitted locally and then added to the model. At the short wavelength side of the Fe edge we additionally adjusted the model to match the continuum level. We observe an Fe K line centered at 1.94 Å, which is consistent with the charge states Fe I–X (e.g., House 1969). The line has an equivalent width of 1.9 mÅ. The spectrum also shows P Cygni lines of Fe XXV and Fe XXVI with the properties given in Table 1. We resolve a neutral Fe edge at 1.75 Å with an optical depth of  $\tau = 0.035 \pm 0.017$ , implying an equivalent hydrogen column density of  $3.4 \times 10^{22}$  cm $^{-2}$ . After subtraction of the interstellar column density, the column densities of neutral and ionized gas appear similar.

Figure 6 (bottom) shows the same spectral region for observation II. The model was calculated in a similar way to that for observation I; however, no correction for pile-up was needed. We detect an Fe K line with a similar position and equivalent width as that observed during observation I. However, we do not see obvious P Cygni lines from Fe XXV and Fe XXVI but mostly resonance absorption with significantly increased equivalent width (see Table 1). The resonance-line positions are the same as observed during observation I indicating little change in velocity. The fact that we do not see much emission from ionized Fe in observation II may at first seem surprising, since we see P Cygni lines in lower  $Z$  ion species. However, if one compares the fluxes of the Lyman  $\alpha$  lines and He-like lines of S, Si, and Mg in Table 1, then the decrease in flux is consistent with that observed in these other ions.

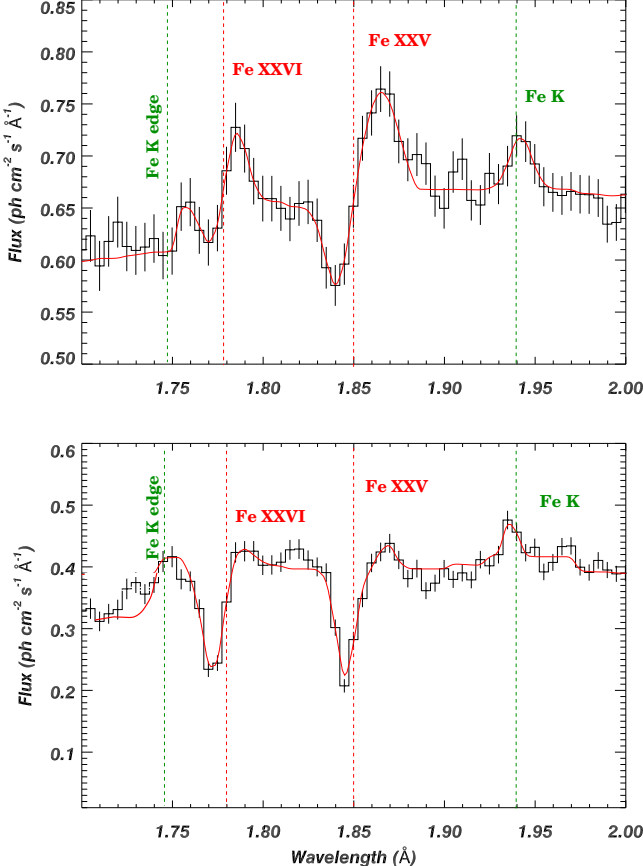


FIG. 6.— Spectral fits of the Fe-K line regions of observation I (top) and observation II (bottom) using the HEG data.

A substantial increase in the depth of the neutral Fe K edge is observed between observation I and observation II. During observation II the depth is  $\tau = 0.108 \pm 0.028$ . To derive this value we had to take into account an unidentified feature at 1.73 Å; because of this feature we had to force the edge to match the high-energy continuum. It is difficult to derive a column density from the edge depth. Due to the partial-covering nature of the absorption and the fact that the neutral absorbing column density is expected to be  $\gtrsim 10^{24}$  cm $^{-2}$  during observation II (see §4.4 of Shirey et al. 1999b), the true column density is likely to be substantially larger than expected from simple consideration of the apparent edge depth. A column density of  $\gtrsim 10^{24}$  cm $^{-2}$  will absorb much of the direct continuum at wavelengths longward of the edge, and due to this “saturation” effect the true depth of the edge (and hence the column density) can be severely underestimated.

#### 4. SHORT-TERM VARIABILITY OF THE LINES

We have also studied short-term variability of the P Cygni lines on time scales within the 30 ks and 15 ks exposure times. To do this, we apply a “sliding-window” technique, where we define a fixed exposure-time window that is sufficiently long to receive a significant signal from the bright lines. At a set of equally spaced times during the observation (separated by a constant “time step”), we then create spectra using the data within the exposure-time window (the exposure-time window is centered on each of the equally spaced times). In the case of observation I, we selected an exposure-time window length of 5 ks and a time step of 1 ks (note that the resulting spectra have some overlap). Within a total exposure time of 30 ks, this allows us to create 24 spectra. Using these spectra, we then cre-

ated three-dimensional “spectral maps” where the  $x$ -axis is the wavelength of each spectrum in 0.015 Å steps, the  $y$ -axis is the time in 1.0 ks steps, and the  $z$ -axis is the photon flux in each pixel.

Figure 7 shows spectral maps for three line regions: the Fe line region (left), the Si XIV Lyman  $\alpha$  line region (middle), and the Mg XII Lyman  $\alpha$  line region (right). The colors represent the flux levels from low (green to black) to high (orange to yellow) on a logarithmic scale. The scale ranges from  $\approx 0.1$ –0.8 ph cm $^{-2}$  s $^{-1}$ . The color changes in these maps in the vertical direction show the variability of the spectra. This variability appears somewhat smoothed since the windows overlap.

The spectral continuum is clearly changing; this is indicated by the large-scale color distribution in each map. At short wavelengths (left map), the continuum stays high throughout most of the observation and then drops rapidly in the last 5 ks. At intermediate wavelengths (middle map), the continuum remains low throughout the first one-third of the observation, increases rapidly around the middle of the observation, and remains high throughout most of the rest of the observation. At longer wavelengths (right map), this trend is continued; the continuum stays low throughout the first half of the observation. This qualitative assessment of the continuum variability is consistent with the *RXTE* results of Shirey et al. (1999a) who find the spectra moving along spectral branches in the X-ray color-color diagram.

The three maps in Figure 7 show that the shapes of the P Cygni lines are highly variable on time scales of 2–3 ks. In the time maps at the top of Figure 7 we observe a correlation of the emission and an anti-correlation of the resonance absorption with the local continuum flux. When the local continuum is low, the emission-line parts of the P Cygni profiles are weak; they grow stronger with increasing continuum flux. The absorption-line parts show the opposite behavior; their amplitudes are larger at lower continuum fluxes, and absorption practically vanishes at high flux levels. This behavior on short time scales reflects the same general pattern we observed by comparing the high-flux state in observation I with the low-flux state in observation II. This also explains why for Fe XXV the emission line reaches its peak flux about 7 ks before we observe the peak in the Si XIV emission line. The line flux is directly connected with the local continuum flux, and in this case the spectral change pattern creates this time difference.

Figure 7 also shows the spectra used to make the spectral maps. The time sequence of the Si XIV line at 6.18 Å shows that the absorption part of the profile has vanished by about 12 ks into observation I, which would imply a column density change of Si XIV from about twice the amount in Table 1 to nearly zero on a time scale of  $\approx 3$  hr. The fact that the flux of the local continuum is anti-correlated with the absorption amplitude suggests that changes in the ionization fraction, rather than changes in column density, are primarily responsible for the changes in absorption strength (although we cannot strictly rule out the latter).

The variability of the Si XIV line during observation II is shown in Figure 8. Although during observation II the overall X-ray flux is substantially lower than during observation I, the ionization parameter appears to be varying over approximately the same range. The emission-line fluxes during observation II, on the other hand, are lower by significant factors (see §3.3).

Figure 8 also illustrates the correlation of spectral hardness and absorption strength for observation II. We computed a hardness ratio by dividing the flux in the 1.7–3 Å band by that in the

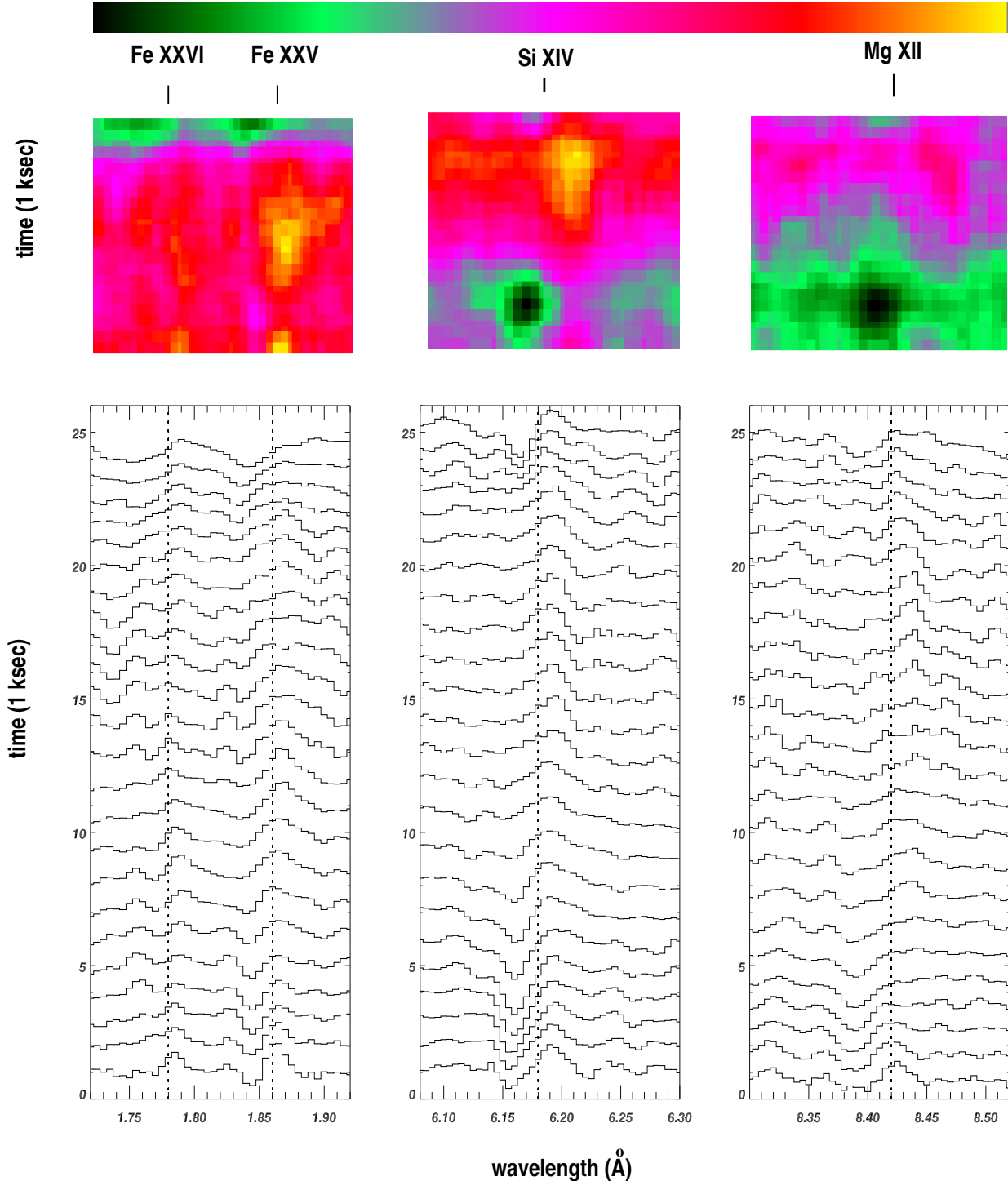


FIG. 7.— Top: Spectral maps of selected regions of observation I: the Fe-line region (left), the Si XIV region (middle), and the Mg XII region (right). Bottom: The spectral profiles from each of the spectral maps above. The time step between each profile is 1 ks.

3–8 Å band; this ratio is similar to the soft-band hardness ratio computed by Shirey et al. (1999b). The flux is computed in the 1.7–8 Å band. We used the same sliding-window technique as used for the spectral maps, and thus in Figure 8 the sequence of data points in the hardness-ratio diagram can be directly matched to the sequence of line profiles. The data points in Figure 8 are connected by dotted lines indicating the time sequence. In the inset of Figure 8 we also plot the softest (spectrum 1) and hardest (spectrum 2) spectra during observation II, which occurred near the beginning and the end of the observation, respectively. Figure 8 shows that while the flux is generally decreasing throughout the observation, the hardness ratio increases until it reaches a plateau at  $\approx 2.3$ . This spectral behavior is consistent with that studied during dip periods with *RXTE* (Shirey et al. 1999b). The more the continuum hardens, the more the absorption in the P Cygni profiles decreases.

During observation I we see similar variations of the P Cygni line on similar time scales. However, here the spectrum is dominated by the soft component, and spectral variations of the hard component cannot be directly measured.

## 5. DISCUSSION

### 5.1. Refined constraints on the accretion-disk wind model

In Paper I we argued that the P Cygni profiles are most likely produced by a high-velocity outflow from an accretion disk viewed in a relatively edge-on manner. The central X-ray source illuminates the disk and produces a wind driven by both thermal and radiation pressure (e.g., Begelman et al. 1983). The intermediate-temperature ( $\sim 5 \times 10^6$  K) part of this wind produces the H-like and He-like X-ray lines (e.g., Raymond 1993; Ko & Kallman 1994) with P Cygni profiles. Our current data remain generally consistent with this scenario, although we recognize that the strong wind variability seen from Cir X-1 is not usually accounted for in the predominantly time-independent theoretical studies; we use these studies as general guides to interpretation rather than for strict comparison purposes.

Our new analyses, combined with other recent work on accretion-disk winds and photoionized plasmas, have allowed us to extend some of the findings in Paper I. For example, one of the potential problems with the disk-wind model noted in §3 of Paper I can now be ameliorated. There we noted that likely values for the wind's launching radius ( $r_{\text{launch}} \approx 10^5$  km), launching density ( $n_{\text{launch}} \gtrsim 10^{15}$  cm $^{-3}$ ), and ionization parameter ( $\xi \lesssim 1000$  erg cm s $^{-1}$ ) led to a wind that was optically thick to electron scattering; most line photons attempting to traverse the wind would then be Compton-scattered out of the line. However, our analysis in §3.4, which uses the calculations of Kallman & Bautista (2001) rather than those of Kallman & McCray (1982), now suggests that a significantly higher ( $\xi \approx 20,000$  erg cm s $^{-1}$ ) ionization parameter is likely for much of the gas creating the P Cygni lines. The required column density along the line of sight is thus correspondingly reduced. Hydrogen column densities of  $\approx 10^{23}$  cm $^{-2}$  can now be accommodated with only moderate shielding of the wind from the full X-ray continuum or clumping of the wind.

The density measurement in the line-emission region of  $\approx 2 \times 10^{13}$  cm $^{-3}$  using the Mg XI triplet (see §3.3) provides a further independent constraint on the disk-wind model. Following the arguments in §3 of Paper I with the new ionization parameter of  $\xi \approx 20,000$  erg cm s $^{-1}$ , the expected launching density is  $n_{\text{launch}} \gtrsim 5 \times 10^{13}$  cm $^{-3}$ . The measured density in the

line-emission region is somewhat, but not greatly, lower than the launching density. Note that since the launching density depends upon the assumed launching radius, the general consistency found above supports our adopted  $r_{\text{launch}} \approx 10^5$  km (chosen to make the observed terminal velocity of the wind comparable to the escape velocity at  $r_{\text{launch}}$ ; see §3 of Paper I).

Gratings observations of other neutron star LMXBs thus far have not generally revealed P Cygni lines as prominent as those observed from Cir X-1 (e.g., Cottam et al. 2001; Marshall et al. 2001; Paerels et al. 2001; Schulz et al. 2001; Sidoli et al. 2001). It is difficult to account for this difference quantitatively, but it may be due to a combination of mass accretion rate (relative to the Eddington rate) and inclination. The high, and perhaps super-Eddington, mass accretion rate of Cir X-1 allows an unusually powerful outflow to be driven from the accretion disk, and a relatively edge-on geometry is optimal for the viewing of an equatorial outflow.

### 5.2. Line and continuum variability

Given the results from *ASCA* and *RXTE* (Brandt et al. 1996; Shirey et al. 1999b), the large difference in overall X-ray flux between observation I and observation II is likely to be due mostly to a change in the amount of absorbing material along the line of sight. As discussed by several authors (see §1), this material is probably associated with a thickening of the accretion disk induced by the strong mass transfer occurring at zero phase. The change in Fe K edge depth observed by *Chandra* is consistent with a large change in the amount of absorbing material, although it is difficult to constrain the exact column density during observation II. The fact that we observe the same basic P Cygni lines during observation I and observation II supports the idea that the underlying ionizing continuum source has not changed dramatically in strength. Furthermore, the fact that the line equivalent widths are significantly larger during observation II than observation I (see Figure 4) is generally consistent with the idea that blockage of direct continuum emission is occurring during observation II. However, it is worth noting that the emission-line fluxes do drop significantly between observation I and observation II (see §3.3). This can be understood without invoking continuum changes if the absorbing material screens ionizing photons from reaching a significant fraction of the line-emitting gas (this screening could be stronger at longer wavelengths, explaining the trend with wavelength noted in §3.3).

However, while it seems clear that changes in absorption play a critical role in causing much of the variability of Cir X-1, some changes in underlying continuum strength and shape are probable as well. These are particularly likely during observation I since it was made while Cir X-1 was undergoing an X-ray flare above its “base” level (see Figure 1 of Paper I). Our data are not ideal for probing the nature of the continuum variability in detail, but Shirey et al. (1999a) have demonstrated that Cir X-1 shows spectral variations that classify it as a “Z” type LMXB. The *Chandra* data strongly suggest that much of the short-term P Cygni line variability is caused by spectral changes in the local continuum which lead to changes in the ionization level of the wind (see §4), although it is difficult to rule out entirely changes in the wind geometry as well. The observed short-term changes of the lines can be dramatic, causing them to vary from being almost completely in absorption to almost completely in emission. Modeling this variability in detail will be a challenge.

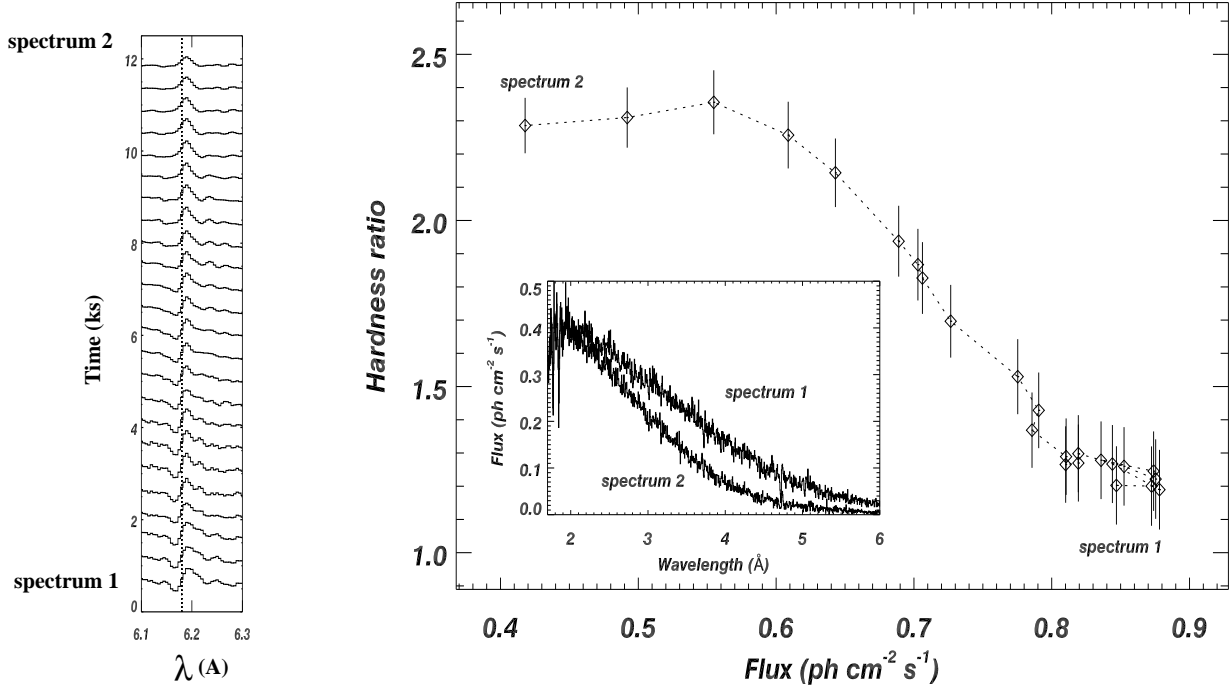


FIG. 8.— Si XIV line profiles and hardness ratio versus intensity plot for observation II. The flux is computed between 1.7 and 8 Å. We used the same sliding-window technique as used for Figure 7. Each data point in the right panel can be directly matched to one of the line profiles in the left panel. The dotted lines connect the data points in order of increasing time. The inset compares the the first (spectrum 1) and the last (spectrum 2) spectra in the sequence.

### 5.3. Comparisons with the spectral features seen from superluminal jet sources

The Fe K line region in the low-flux state spectrum of Cir X-1 shows strong, blueshifted resonance absorption features from Fe XXV and Fe XXVI. Significant line emission during the low-flux state is only seen from neutral or nearly neutral Fe. Such spectral behavior is reminiscent of that seen from Galactic superluminal jet sources containing a black hole like GRS 1915+105 (Kotani et al. 2000; Lee et al. 2001) and GRO J1655–40 (Ueda et al. 1998; Yamaoka et al. 2001). Similar Fe absorption has also now been observed in GX 13+1 (Ueda et al. 2001), a neutron star LMXB that has been classified as an atypical atoll source (Hasinger & van der Klis 1989), and MXB 1659–298 (Sidoli et al. 2001), also probably an atoll source; these results show that these spectral features can appear independent of the nature of the compact object and the existence of jets. In most of these cases it has been argued that the absorption lines come from a highly ionized plasma layer extending to large heights above the equatorial plane (Yamaoka et al. 2001). Specifically, a geometrically thick accretion flow at  $\sim 10^4$  Schwarzschild radii is assumed, which in the case of GRO J1655–40 amounts to  $\sim 10^5$  km. This is of the same magnitude as our launching radius for the wind in Cir X-1, and it is

worth considering the possibility that the material creating the Fe X-ray absorption lines in superluminal sources might generally be outflowing rather than inflowing. An equatorial wind scenario appears consistent with the gratings observations of GRS 1915+105 (Lee et al. 2001); if the outflow velocity for GRS 1915+105 is assumed to be the same as that for Cir X-1, the outflow would need to be less inclined relative to the line of sight to be consistent with the 770 km s<sup>-1</sup> upper limit on the blueshift. The strong Fe XXVI absorption feature from GRS 1915+105 shows variations on similar time scales to those observed from Cir X-1.

Superluminal jet sources containing black holes have not shown as many spectral features as we observe from Cir X-1; typically only features from highly ionized iron are seen. This could plausibly be explained if their winds are more highly ionized due to their larger luminosities and different continuum shapes, so that iron is the only abundant element not fully stripped of its electrons.

We thank all the members of the *Chandra* team for their enormous efforts. We gratefully acknowledge the financial support of CXC grant GO0-1041X (WNB, NSS) and Smithsonian Astrophysical Observatory contract SV1-61010 for the CXC (NSS).

### REFERENCES

Bautista, M.A., & Kallman, T.R. 2000, ApJ, 544, 581  
 Begelman, M.C., McKee, C.F., & Shields, G.A. 1983, ApJ, 271, 70  
 Blundell, K.M., Mioduszewski, A.J., Muxlow, T.W.B., Podsiadlowski, P., & Rupen, M.P. 2001, ApJ, in press (astro-ph/0109504)  
 Brandt, W.N., Fabian, A.C., Dotani, T., Nagase, F., Inoue, H., Kotani, T., & Segawa, Y. 1996, MNRAS, 283, 1071  
 Brandt, W.N. & Schulz, N.S. 2000, ApJ, 544, L123  
 Case, G.L., & Bhattacharya, D., 1998, ApJ, 504, 761  
 Chiang, J. 2001, ApJ, 549, 537  
 Cerdova, F.A., & Howarth, I. 1987, in *Exploring the Universe with the IUE Satellite*, eds. Y. Kondo et al. (Dordrecht: D. Reidel), p. 395  
 Cottam, J., Kahn, S. M., Brinkman, A. C., den Herder, J. W., & Erd, C. 2001, A&A, 365, L277

Fender, R., Spencer, R., Tzioumis, T., Wu, K., van der Klis, M., van Paradijs, J., & Johnston, H. 1998, *ApJ*, 506, L121

Glass, I.S. 1994, *MNRAS*, 268, 742

Hasinger, G.R., & van der Klis, M. 1989, *A&A*, 225, 79

Iaria, R., Burderi, L., Di Salvo, T., La Barbera, A., & Robba, N.R. 2001a, *ApJ*, 547, 412

Iaria, R., Di Salvo, T., Burderi, L., & Robba, N.R. 2001b, *ApJ*, 561, 321

Johnston, H.M., Fender, R., & Wu, K. 1999, *MNRAS*, 308, 415

Johnston, H.M., Wu, K., Fender, R., & Cullen, J.G. 2001, *MNRAS*, 328, 1193

Kallman, T.R., Liedahl, D.A., Osterheld, A.L., Goldstein, W.H., & Kahn, S.M. 1996, *ApJ*, 465, 994

Kallman, T.R., & Bautista, M. 2001, *ApJS*, 133, 221

Kaluzienski, L.J., Holt, S.S., Boldt, E.A., & Serlemitsos, P.J. 1976, *ApJ*, 208, L71

Kotani, T., Ebisawa, K., Dotani, T., Inoue, H., Nagase, F., Tanaka, Y., Ueda, Y., 2000, *ApJ*, 539, 413

Lee, J.C., Reynolds, C.S., Remillard, R., Schulz, N.S., Blackman, E.G., & Fabian, A.C. 2001, *ApJ*, in press (astro-ph/0111132)

Liedahl, D.A., Sako, M., Paerels, F., Mc Collough, M. L., Elsner, R.F., Schulz, N.S., & Cohen, D.H. 2000, *HEAD*, 32.2503

Marion, B., Lampton, M., Bowyer, S., & Crudeace, R. 1971, *ApJ*, 169, L23

Marshall, H.L., et al. 2001, *ApJ*, 122, 21

Mewe, R. 1994, *SPEX* Version 1.0/Rev. 4.0

Mignani, R., Caraveo, P.A., & Bignami, G.F. 1997, *A&A*, 474, 51

Miller, J. M., Fabina, A.C., Wijnands, R., Remillard, R.A., Wojdowski, P., Schulz, N.S., DiMatteo, T., Marshall, H.L., Canizares, C.R., Pooley, D., and Lewin, W.H.G., 2002, *ApJ*, submitted

Mirabel, I.F. 2001, *Ap&SS*, 276, 319

Moneti, A. 1992, *A&A*, 260, L7

Morrison, R., & McCammon, D. 1983, *ApJ*, 278, 1082

Paerels, F., Brinkman, A.C., van der Meer, R.L., Kaastra, J.S., Kuulkers, E., Boggende, A.F.den, Predehl, P., Drake, J.J., Kahn, S.M., Savin, D.W., and McLaughlin, B.M., 2001, *ApJ*, 546, 338

Porquet, D., & Dubau, J. 2000, *A&AS*, 143, 495

Predehl, P., & Schmitt, J. H. M. M., 1995, *A&A*, 293, 889

Proga, D., & Kallman, T.R. 2001, *ApJ*, 565, 455

Qu, J.L., Yu, W., & Li, T.P. 2001, *ApJ*, 7

Raymond, J.C. 1993, *ApJ*, 412, 267

Schulz, N.S., Hasinger, G.R., & Trümper, J. 1989, *A&A*, 225, 48

Schulz, N.S., & Brandt, W.N. 2001, in *X-ray Astronomy 2000*, Eds. R. Giacconi, L. Stella, and S. Serio, ASP conference series, in press

Schulz, N.S., Chakrabarty, D., Marshall, H.L., Canizares, C.R., Lee, J.C., & Houck, J. 2001, *ApJ*, 563, 941

Shirey, R.E., Bradt, H.V., & Levine, A.M. 1999a, *ApJ*, 517, 472

Shirey, R.E., Levine, A.M., & Bradt, H.V. 1999b, *ApJ*, 524, 1048

Stewart, R.T., Nelson, G.J., Penninx, W., Kitamoto, S., Miyamoto, S., & Nicolson, G.D. 1991, *MNRAS*, 253, 212

Sidoli, L., Oosterbroek, T., Parmar, A.N., Lumb, D., & Erd, C. 2001, *A&A*, 379, 540

Stewart, R.T., Caswell, J.L., Haynes R.F., & Nelson, G.J. 1993, *MNRAS*, 261, 593

Tauris, T.M., Fender, R.P., van den Heuvel, E.P.J., Johnston, H.M., & Wu, K. 1999, *MNRAS*, 310, 1165

Tennant, A.F., Fabian, A.C., & Shafer, R.A. 1986, *MNRAS*, 221, 27

Ueda, Y., Asai, K., Yamaoka, K., Dotani, T., & Inoue, H. 2001, *ApJ*, 566, L87

Whelan, J.A.J., et al. 1977, *MNRAS*, 181, 259

Wilms, J., Allen, A., & McCray, R. 2000, *ApJ*, 542, 914

Yamaoka, K., Ueda, Y., Inoue, H., Nagase, F., Ebisawa, K., Kotani, T., Tanaka, Y., & Zhang, S.N., 2001, *PASJ*, 53, 179